



Residual stresses induced by electron beam welding in a 6061 aluminium alloy



D. Bardel^{a,b,c,*}, D. Nelias^a, V. Robin^c, T. Pirling^d, X. Boulnat^b, M. Perez^b

^a Université de Lyon, INSA-Lyon, LaMCoS UMR CNRS 5259, F69621 Villeurbanne, France

^b Université de Lyon, INSA-Lyon, MATEIS UMR CNRS 5510, F69621 Villeurbanne, France

^c AREVA NP, Département d'ingénierie mécanique, Lyon, France

^d Institut Laue Langevin, ILL-Grenoble, F 38042 Grenoble, France

ARTICLE INFO

Article history:

Received 19 October 2015

Received in revised form 8 April 2016

Accepted 9 April 2016

Available online 11 April 2016

PACS:

81.40.Gh

81.05.Bx

61.05.fm

02.70.Dh

81.05.Rm

81.40.-z

Keywords:

Thermo-metallurgical analysis

6061 Aluminium alloy

Neutron diffraction

Finite elements

Residual stresses

EBSD

ABSTRACT

Electron beam welding fusion line was performed on 6061-T6 aluminium plates. The thermal histories encountered in the heat affected zone were measured to calibrate a thermal finite elements model. This model has been used as entry parameter of a metallurgical model that predicts the precipitation dissolution induced softening, as well as residual elastic strains. Local deformations measured with a neutron diffraction experiment show a good agreement with the coupled modelling approach for all strain components and the "M" shaped residual strain curves, characteristic of age hardening alloys weld joints, is well reproduced.

© 2016 Elsevier B.V. All rights reserved.

1. Introduction

The modelling of welding processes is complex because it involves many coupled phenomena at various scales as described in Debroy and David (1995) work (fluid dynamics, heat transfer, solidification, precipitation, etc). Not only the molten zone (MZ) is affected by the welding process, but also many microstructural transformations may occur in the so-called heat affected zone (HAZ) inducing important consequences on the final properties of the welded parts. Among all these properties, residual stresses strongly affect the distortion and fatigue life of structures (Costa et al., 2010), the toughness and the corrosion resistance in welds (Deplus et al., 2011). The

prediction of residual stresses involves a fine coupling of all these approaches.

The simulation of the dynamics of the MZ uses various physical fields such as fluid dynamics (Traidia and Roger, 2011), heat transfer, chemistry and electromagnetism (Traidia et al., 2013) to predict the shape of the MZ and the amount of energy absorbed by the sample to consequently estimate the size of the HAZ.

Microstructural models (i.e. solidification Rappaz and Gandin, 1993 or precipitation Perez et al., 2008) can be used to predict the solidification patterns Mokadem et al. (2007), Wang et al. (2004) and also the precipitation state Simar et al. (2012) within the MZ and the HAZ.

To the best of authors knowledge, despite their fine description of microstructural features, multi-physical models do not go so far as to predict residual stresses. This is due to high computational cost and/or wide range of experimental data needed to validate their consistency.

* Corresponding author.

E-mail addresses: didier.bardel@insa-lyon.fr (D. Bardel), daniel.nelias@insa-lyon.fr (D. Nelias).

Table 1

Chemical composition of the 6061 aluminium alloy used for the welding experiments.

	Mg	Si	Cu	Fe	Cr	Mn	Oth.
wt%	1.02	0.75	0.25	0.45	0.05	0.06	0.09
at%	1.14	0.72	0.11	0.22	0.03	0.03	0.04

At the other hand, mechanical approaches are based on the estimation of local constitutive laws by reproducing the thermal cycle of a given region on a macroscopic sample (e.g. using thermomechanical simulator). Finite element codes interpolate the experimentally characterised constitutive laws to predict residual stresses (see the recent contribution of Chobaut et al., 2015). However, these approaches depend on the geometry of the parts: a new geometry would require new set of mechanical characterisation.

To by-pass this difficulty, a simple thermo-metallurgical approach is proposed in this paper: a thermal model based on the equivalent heat source Goldak et al. (1984) is first used to reproduce the size of the MZ/HAZ and the evolution of the thermal field. From this field, a microstructural model predicts the proportion of hard and soft phases that is, itself implemented in a FE software that predict residual stresses.

2. Electron beam welding experiments

2.1. Materials and treatments

6061 Alloy is a high strength aluminium alloy thanks to a specific heat treatment (presented for example in Bardel et al., 2014) to obtain the largest density of hardening β'' precipitates (i.e. T6 state). The composition of the alloy, where several thermocouples are fixed, is given in Table 1. In order to mimic real welding experiment and also get reproducible results, a fusion line was performed on two 6061-T6 plates: the first one was used for microstructure analysis and the second one for residual stress analysis.

The first objective of the modelling of the thermal field within the whole plate is the calibration of an equivalent heat source. The work of Zain-Ul-Abdein et al. (2010) has shown that only a limited number of well placed thermocouples are required for this calibration. Thus, 7 ThermoCouples (TC) (referred as TC1–TC7) were positioned in the lower and upper surface of the plate and 3 additional TC (referred as TC8–TC10) were used to check the reproducibility of the approach (see Fig. 1). K-type thermocouples (diameter 80 μm) are micro-welded on upper and lower surfaces. Then, varnish is filled on the contact area to protect the connection against mechanical stresses and to get more accurate thermal measurement by limiting radiation effects from the beam. The thermocouples are linked to a Nimtech FrontDAQ acquisition central thanks to air and electric-proof connections. To get accurate results, even for fast heating rates, the acquisition frequency is 200 Hz. The response time of the whole equipment have been measured and it is 15 ms for a simulated increment of temperature $\Delta T = 400^\circ\text{C}$.

These experiments were performed at the IUT of Creusot (France). The electron beam (EB) welding device has a power of 5.47 kW ($U=55.9\text{ kV}$, $I=97.8\text{ mA}$) with a vacuum pressure in the gun of about 10^{-5} hPa . The maximal dimensions for the welded plates in the chamber (where the vacuum pressure is $5 \times 10^{-3}\text{ hPa}$) are $=180 \times 200\text{ mm}$ (length and width) and they are laid on rectangular parallelepipeds.

From 30 mm thickness cold rolled workpiece, upper and lower surfaces have been machined (well lubricated) in order to get a thickness of 20 mm and thus assure full penetration of the welds. This protocol has been set to eliminate the shear texture surface effect resulting from rolling as described in Delannay and Mishin (2013). Textured sample are indeed not well suited for residual

stresses measurement by diffraction methods, since too few grains in the gauge volume (GV) may lead to no diffraction signal.

To evaluate the influence of the welding velocity V on residual stresses, several tests were performed with $V=0.45\text{ m/min}$, $V=0.72\text{ m/min}$ and $V=0.9\text{ m/min}$. For each velocity, one plate (the one used for diffraction) were instrumented with TC and the other (the one used for microstructure analysis) were welded in the exact same conditions.

In this paper, most of the experimental and numerical results are presented for the $V=0.45\text{ m/min}$ plate because this low velocity induces more drastic changes in the precipitation state.

The fusion line experiment is composed of four steps: (i) starting outside the specimen with low velocity until the plate border, (ii) fusion line in the plate with a constant velocity and extinction outside the sample, (iii) cooling in the vacuum chamber during $\approx 5\text{ min}$ and finally (iv) cooling in the lab environment.

2.2. Thermal results

The temperature profile of all TC is reported in Fig. 12. These results do not show the final cooling stage when vacuum is broken. Thermal profiles are in phase for the upper and lower surfaces except for TC9/TC10 thermocouples that have been fixed at a distance of 120 mm from the starting point unlike the others that are welded at a distance of 60 mm (cf. Fig. 1). Temperature profiles of TC9/TC10 are similar to TC6/TC7, which attests that steady state conditions are fulfilled during welding.

For a same transverse distance from the weld centre, the thermal gradients are more important in the upper surface. This demonstrates the energy gradient through the thickness and justify a conical repartition of the equivalent heat source.

Heating (HR) and cooling (CR) rates are defined as the time lap between 50°C and the maximum temperature, and the maximum temperature and 150°C , respectively. The highest gradient was measured by TC4 (HR = 158°C/s , CR = 32.9°C/s), which has been fixed at 3.5 mm from the weld centre (cf. Fig. 1).

After approximately one minute from the beginning of the process there is no more significant temperature gradient in the plate. At this stage the cooling rate is low in the vacuum chamber (CR $\approx 0.07^\circ\text{C/s}$), then after opening the chamber CR increases by convection (CR $\approx 0.15^\circ\text{C/s}$) and this effect is amplified when the plate is put outside the welding instrument.

3. Experimental investigations

3.1. Macrographic analysis

To calibrate finite element (FE) thermal modelling (presented in the next section), the size of the molten zone (MZ) must be determined. Thus, to distinguish between the various zones in the welds, macrographic specimen were cut, polished and etched with Keller reagent and then observed with a LEICA M420 optical microscope (zoom $\times 3$). A picture is provided for each welding velocity in Fig. 2 for samples collected in the central section of the plates.

On the cross sections shown in Fig. 2, the MZ is clearly distinguishable. Note that the transition between the HAZ and the BM cannot be distinguished in such macroographies; only a transmission electron microscopy (TEM) study could bring more information about the boundary of the HAZ from a precipitation point of view.

3.2. Scanning electron microscopy

To get more insight into the microstructural evolution in the welds, a scanning electron microscopy (SEM) study was performed. A Field Emission Gun SEM Zeiss Supra 55VP (diaphragm diameter

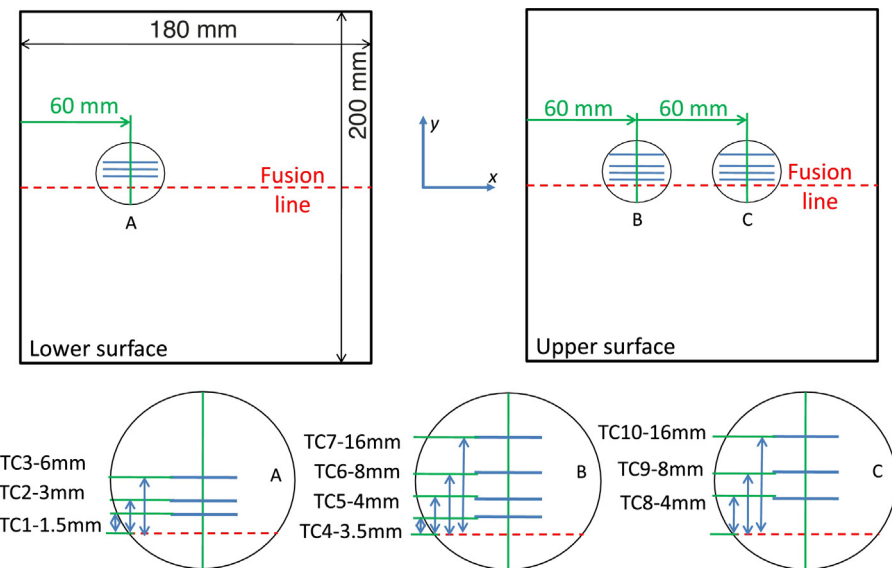


Fig. 1. Thermocouples position for the plate welded with $V = 0.45 \text{ m/min}$.

60–120 μm) equipped with a secondary and backscattered electrons detector was used. Chemical analyses were performed using an energy dispersive X-ray analyzer.

SEM observations performed on different places around the weld (Fig. 3) highlight the presence of white and black objects with various morphologies depending on the zone. These white and black phases are finely distributed in the MZ (particularly at grain boundaries) compared to BM where there are coarser and more aligned. These phases have been identified as the intermetallics iron (white phase) and coarse Mg₂Si precipitates (black phase) (see Fig. 3). These phases are well known in the 6061 alloys. Shen et al. (2013) show that their presence is detrimental to the toughness of the alloy.

SEM measurements have been enriched with the support of electron backscatter diffraction (EBSD) analysis. They have been conducted on a narrow weld (lower part of the 0.9 m/min velocity

weld) to get pictures that show simultaneously the granular structure of the MZ and the HAZ. During solidification, the velocity of the solid/liquid front and temperature gradients magnitude have a preponderant influence on the formation of the grain structure (see Hunt, 1984).

Welding induces thermal gradients emphasised by characteristic columnar structure developed in the gradient direction. With no gradient, an equiaxed structure is observed. In Fig. 4, the molten zone exhibits a columnar structure (plus a few equiaxed grains), in contrast with the HAZ, where grains are large and equiaxed.

The grains orientations shown in Fig. 4 do not reveal any local crystallographic texture. Moreover, the intragranular orientation gradient determined by kernel average misorientation (KAM) (Calcagnotto et al., 2010) (see example of maps in Boulnat et al. (2014)) is shown in Fig. 4: there is no pronounced misorientation (linked to geometrically necessary dislocations). These

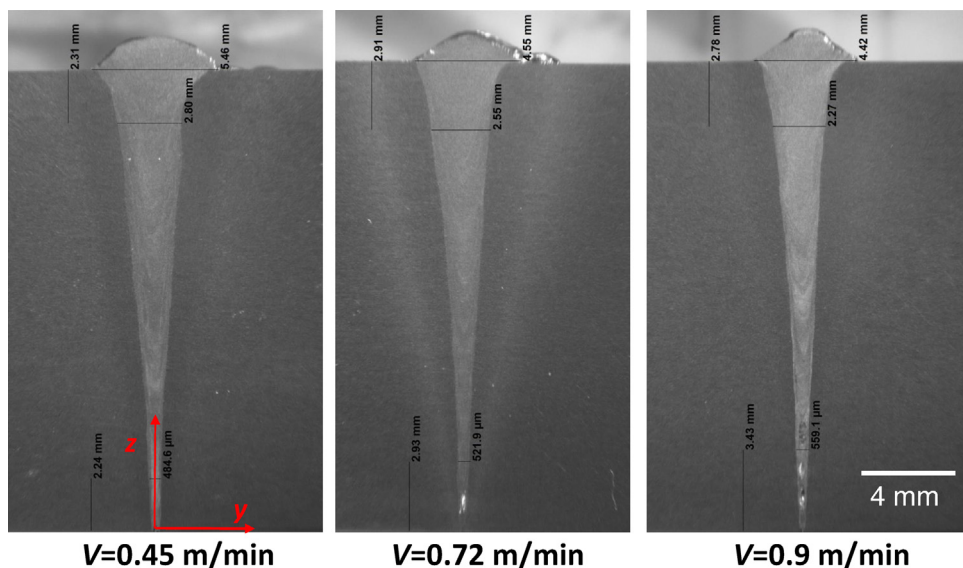


Fig. 2. Macrographic cuts obtained by optical microscopy for plates welded at three different velocities.

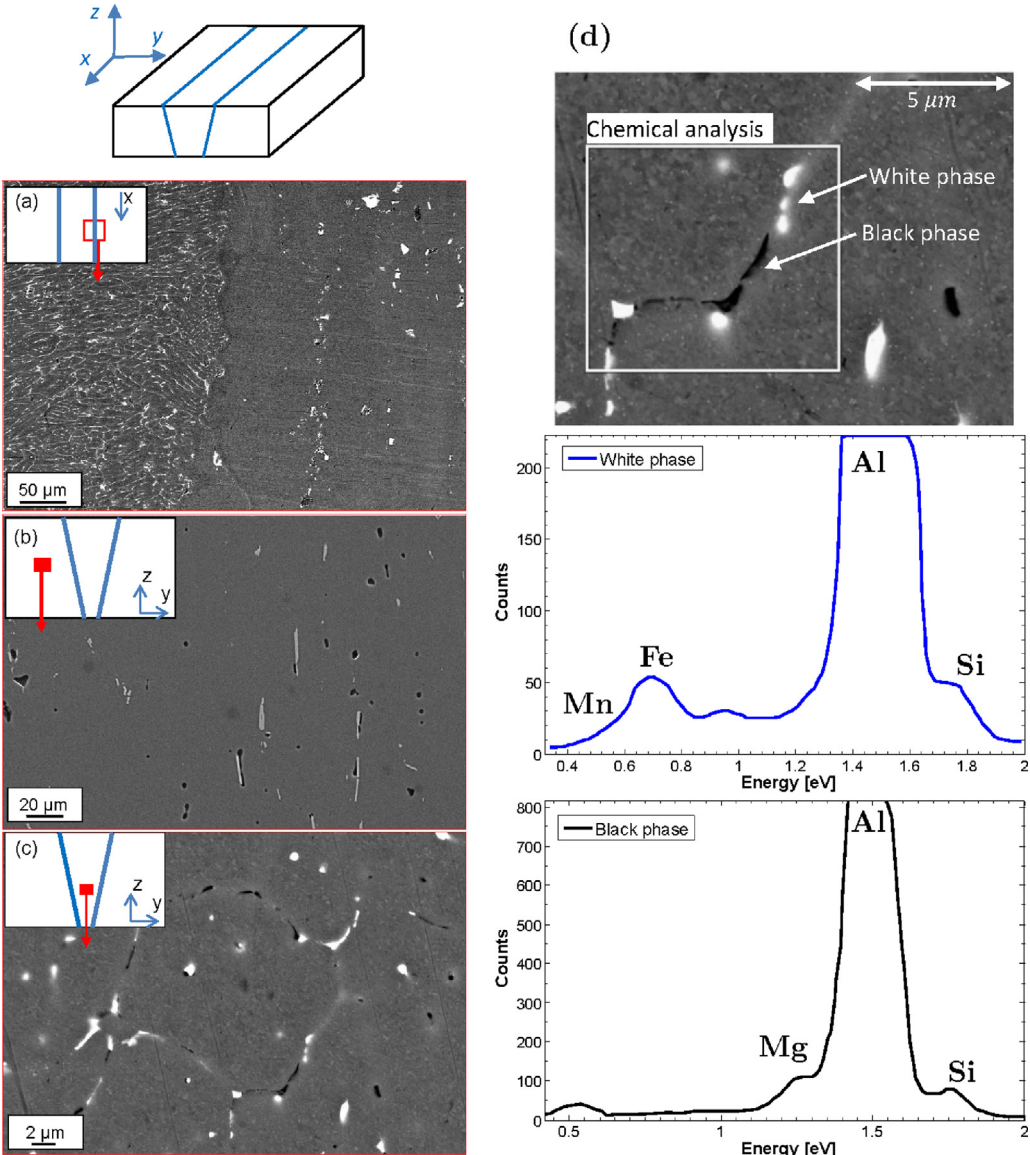


Fig. 3. SEM microographies showing intermetallics (white) and coarse precipitates (black) in: (a) both the heat affected zone (HAZ) and the molten zone (MZ) top view; (b) the BM; (c) the MZ. The white phases are much coarser in the BM than in the MZ. (d) Chemical analysis performed on coarse phases.

results confirm the good disposition of the sample to measure residual deformations: no texture nor significant intragranular heterogeneities (which could lead to III order stresses unmeasured by diffraction).

3.3. Neutron diffraction

Among all possible methods to estimate residual stresses (see the review of Rossini et al., 2012), neutron diffraction (ND) have many advantages: it can easily scan welded plates through the thickness while having a fine resolution. Moreover, it is rather insensitive to surface roughness. This direct residual strain method was performed in the Laue Langevin Institute (ILL) at Grenoble on the SALSA instrument presented in Pirling et al. (2006). This device uses a high neutrons flux and the measurements are weakly affected by the background noise that is low on this instrument (Acevedo et al., 2012). SALSA is a neutron diffraction instrument designed for the determination of lattice strains

$\varepsilon = (d_{hkl} - d_{hkl}^0)/d_{hkl}^0$ relying on an accurate measurement of the inter-reticular distances d_{hkl} which plays the role of deformation gauge for a material under stresses.

When a neutron flux is projected into a material, neutron diffusion and interference lead to diffraction peaks at particular 2θ angles with respect to the Bragg's law:

$$n\lambda = 2d_{hkl} \sin(\theta) \quad (1)$$

where n is the diffraction order and λ is the wavelength.

To deduce the average inter-reticular distance d_{hkl} from diffraction angle 2θ , two kinds of method are available: "polychromatic time of flight" and "monochromatic angular dispersive". The first is particularly suited for monitoring phase transformations. It consists in getting a multitude of diffraction peaks and the wavelength by the time of flight method. The second approach, that is used on SALSA and described in Withers (2007), is well suited to measure macroscopic stresses: only one diffraction peak 2θ is recorded with a monochromatic wavelength (here $\approx 1.64 \text{ \AA}$). We chose the (311)

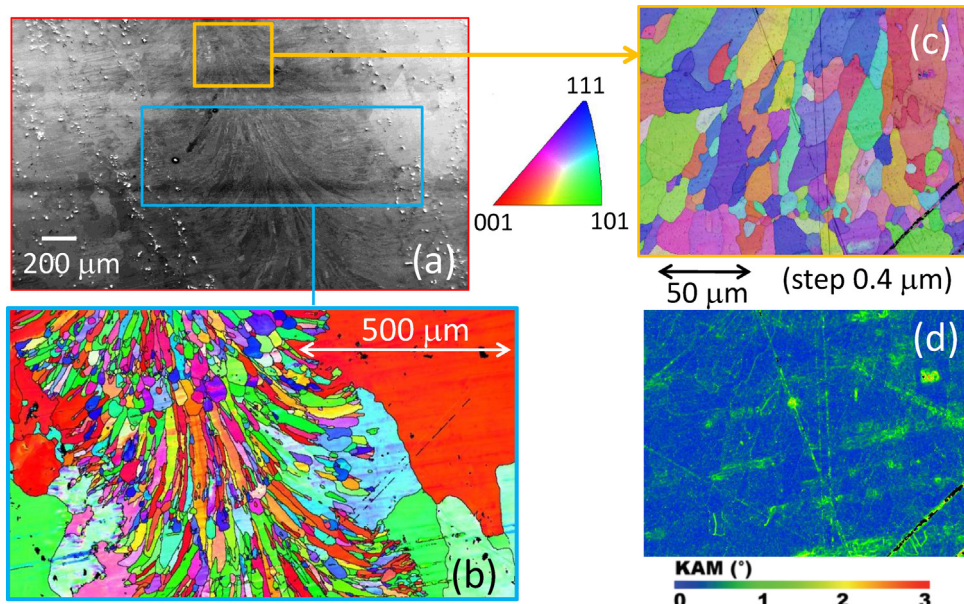


Fig. 4. Top view of the weld performed at a depth of 16 mm. (a) Global illustration of the longitudinal section (b) with its associated EBSD cartography in inverse pole figure. (c) Zoom on the EBSD cartography in the MZ with, (d) its associated local intragranular misorientation (KAM). This sample is suitable for residual deformations measurement: no texture nor significant intragranular heterogeneities are observed.

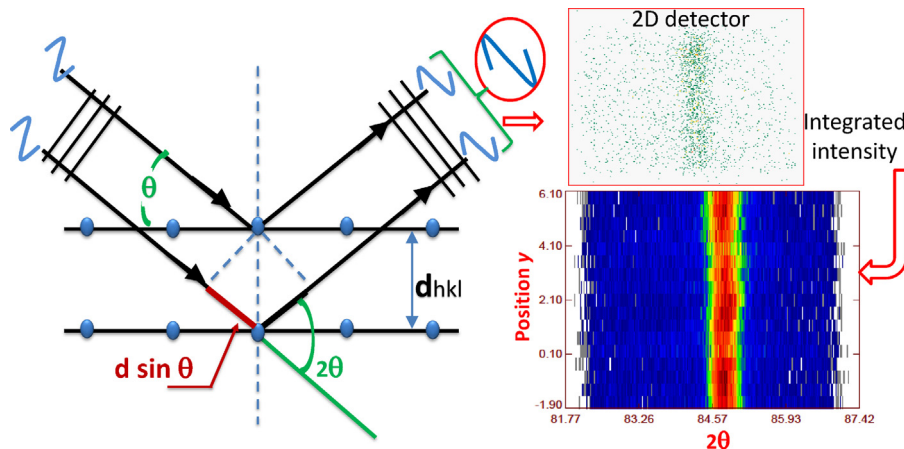


Fig. 5. Illustration of (a) the Bragg's law and typical results from SALSA instrument: (b) intersection of between diffracted cone and 2D detector, and (c) integrated intensity along the y-axis.

planes because they do not accumulate significant inter-granular stresses and therefore exhibit the behaviour of bulk (see also Drezet et al., 2012's contribution). In addition, the 2θ peak is close to 90° (see Fig. 5) leading to a gauge volume (GV) that can be assimilated to a parallelepiped.

From the diffraction peak, an average 2θ position is recorded and deformations or stresses can be deduced by comparison with a free sample. Here, only first order stresses can be deduced (homogeneous stress state on a grain aggregate).

3.4. Diffraction measurements

Generally the diffraction vector K (cf. Fig. 6), which provides the direction of the strain is chosen in three orthogonal directions to deduce the diagonal values of the strain tensor. Here, diffraction peaks are recorded in longitudinal, transverse and normal directions of the weld (c.f. Fig. 6). The optimal size of the gauge volume (GV) depend on two main factors:

- the strain gradient characteristic size, which is expected in the structure. On the cross sections of Fig. 2, the size of the MZ is about 0.5 mm close to weld root. Then, a classical section $2 \text{ mm} \times 2 \text{ mm}$ for the GV should be avoided.
- the allocated beam time: the lower the GV is, the weaker the diffracted neutrons flux will be. However, to have a statistically good diffraction peak the count number on the detector (cf. Fig. 5) has to be as high as possible.

From the size of the zones in Fig. 2, a $0.6 \text{ mm} \times 0.6 \text{ mm}$ section was chosen for the GV in normal and transverse directions (then the resolution is about 0.849 mm). This section being very low, the counting time to obtain a reliable diffraction peak is large (≈ 30 – 40 min for one direction). In addition, to capture strain gradients, overlap measurements were chosen. So it was decided to chose a beam width of 20 mm in order to reduce the acquisition time. This dimension may seem important, nevertheless in normal and transverse directions the width of the beam coincides with

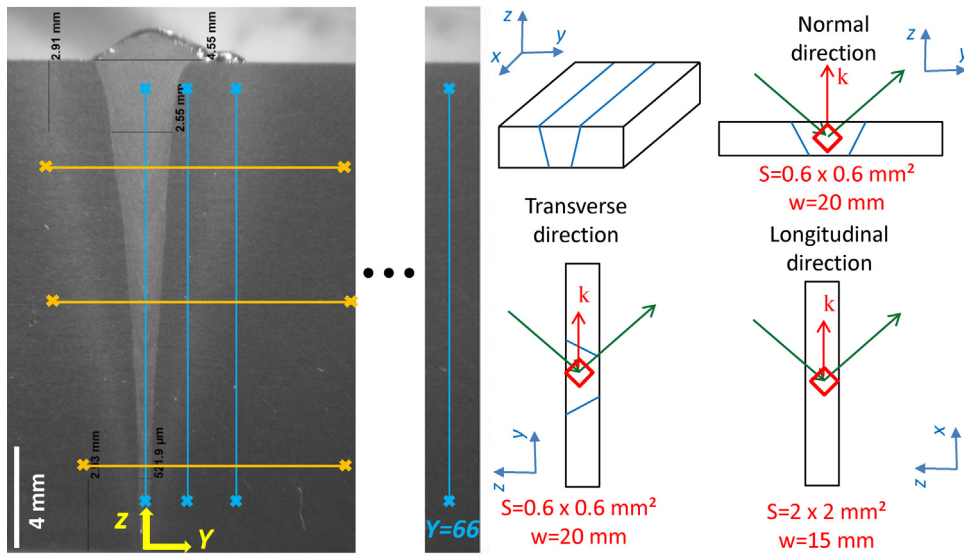


Fig. 6. (a) Lines scanned by the neutron beam for local strain measurement (cross symbols are the beginning and the end of each investigated lines). (b) Representation of the several gauge volume for each orientation of the place. S and w denote the section and the width of the gauge volume.

the longitudinal x -direction of the weld joint (Fig. 6) for which quasi steady state is expected (regarding stress distribution and the boundary conditions that prevent rigid body motions). Thus a quasi homogeneous mechanical behaviour is expected for a very reasonable acquisition time (≈ 7 min per point). In the longitudinal direction, the GV section is less restrictive but the width of the beam must remain moderate. Therefore, it was reduced to 15 mm and a $2 \text{ mm} \times 2 \text{ mm} \times 15 \text{ mm}$ GV was chosen (Fig. 6).

Measurements obtained on the 2D SALSA detector were analysed using the beam line software: LAMP. The diffracted intensities I are integrated to obtain a unidirectional diffraction peak ($I(2\theta)$). Background noise correction and a Gaussian fitting are then performed to deduce the 2θ position. For most of the results, the error bar provided by the adjustment procedure (given by LAMP) is very low.

For the sake of accuracy, in the longitudinal direction, three different rotation angles ($\pm 1.5^\circ$) have been used and diffraction data have been summed up. In spite of this particular procedure, the statistics related to the longitudinal direction remained poorer than the transverse and normal directions. This effect cannot be attributed to a crystalline texture effect, but is probably due to (i) a too low counting time or, (ii) a columnar grain structure that limits the number of diffracted grains (cf. Fig. 4)

3.5. Residual elastic strains results

To get the residual elastic deformations $\varepsilon = \Delta d_{hkl}/d_{hkl}^0$, the variation of inter-reticular distance (or diffraction peak) must be performed. On SALSA, the wavelength λ can be assumed constant, the derivative of Bragg's law provides:

$$\varepsilon = -\frac{\Delta 2\theta}{2 \tan(\theta)} \quad (2)$$

where $\Delta 2\theta$ is the peak displacement (from $2\theta_0$) for the same alloy without stresses and with the same local composition. To have a good reference value $\Delta 2\theta_0$ and to deduce $\Delta 2\theta$, measurements were performed on a superposition of thin "combs" (thickness 1 mm and width 1.5 mm), which were cut from a section in the welded plate (see Fig. 7). This structure allows to relax residual stresses to get a reference that best approximates a mechanical stress free state. Then, measurements were performed in the MZ, HAZ and the BM of the combs to overcome the chemical composition influence. An expansion of the lattice from the BM to the HAZ was observed (a dissolution of precipitates induces in the matrix a homogeneous presence of many solutes atoms) and a slight compression from the HAZ to the MZ (probably due to the smaller grain size whose boundaries traps many atoms and

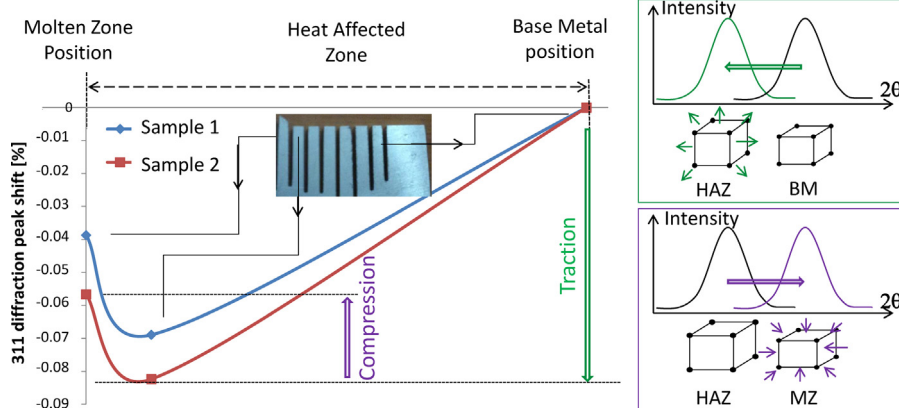


Fig. 7. Combs used for the reference stress free state and representation of the chemical effect on the peak position 2θ for two identical reference samples.

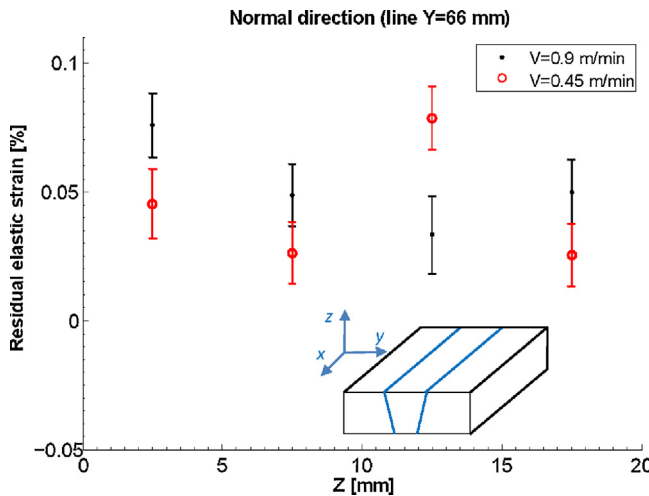


Fig. 8. Residual elastic strains far from the weld for plates welded with $V=0.45 \text{ m/min}$ and $V=0.9 \text{ m/min}$.

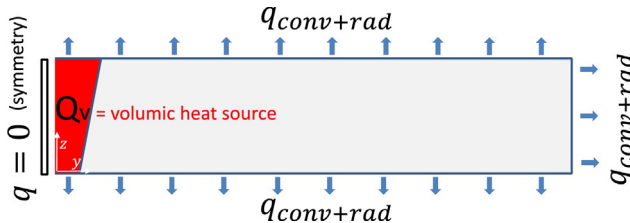


Fig. 9. Representation of boundary conditions heat fluxes and internal heat source.

intermetallic (cf. Fig. 3) and therefore generates less intragranular expansion).

The elastic strain measurements in the normal direction performed at a distance of $y=66 \text{ mm}$ for the weld is shown in Fig. 8. It demonstrates that residual deformations are not zero in the BM far away from the weld. This effect can be caused by rolling process. The numerical simulations presented in the next section suggests that this residual strain state away from the weld should be zero if forming process is ignored. Thus, a weak shift on the diffraction peak (0.5% of the current value) was performed to have in average 0% strain far from the weld (see Figs. 8 and 9).

Figs. 14 and 15 show the results of residual elastic strains in three different directions for two plates: $V=0.45 \text{ m/min}$ and $V=0.9 \text{ m/min}$. It is important to note that the error bars presented in these figures represent only the error caused by the adjustment procedure and not the whole possible sources of errors (e.g. misalignment, microstructure "defects", instrumental resolution).

The transverse line results show a typical "M" profile for the residual strain, as mentioned by Sonne et al. (2013). This profile is characteristic of the softening induced by the dissolution of precipitates close to the weld centre. The strain amplitude is lower in the normal and transverse directions. These results are close to Zain-Ul-Abdein et al. (2009) ones obtained during the laser welding process of thin plates gotten by finite element simulations for a 6056 aluminum alloy.

3.6. Residual strains and stresses

Strain measurements have been carried out in three orthogonal directions in several areas of the weld. Using Hooke's law ($\sigma_{ij}=\lambda\varepsilon_{kk}\delta_{ij}+2\mu\varepsilon_{ij}$) leads to the determination of the diagonal terms of the stress tensor σ_{ij} with the elastic Lame coefficients (λ , μ) relying to longitudinal, transverse and normal residual strain

measured with neutron diffraction. Note that the shear components of the stress tensor cannot be determined.

It should be noted that this strain to stress conversion can be a source of errors: (i) CFC structure is not isotropic; (ii) the possible local texture (or large grain sampling) is not accounted in the isotropic elastic constants E and ν , (iii) the stress calculation is performed from measurements with different accuracy and GV (i.e. longitudinal strain measurements are less accurate than normal and transverse measurements).

This is why, in this work, only the residual elastic strains are compared with the EB simulation results thanks to Sysweld software.

4. Finite element thermal analysis

4.1. Thermal analysis

The first objective for the numerical simulation of welding is to predict the temperature field across the welded plate. Thus an equivalent heat source approach has been selected. This kind of methodology allows to reduce a complex multi-physical problem to a thermal problem that can be modelled by the following heat equation:

$$\rho(T)C_p(T)\frac{\partial T}{\partial t} - \nabla \cdot (\lambda(T)\nabla T) - Q_v = 0 \quad (3)$$

where ρ , C_p , λ and Q_v are the density [kg m^{-3}], the heat capacity [$\text{J kg}^{-1} \text{K}^{-1}$], the thermal conductivity [$\text{W m}^{-1} \text{K}^{-1}$] and an equivalent internal heat source [W m^{-3}]. This equation can be written as a function of enthalpy $H(T) = \int_{T_0}^T C_p(u)du$:

$$\frac{\partial(\rho(T) \cdot H(T))}{\partial t} - \nabla \cdot (\lambda(T) \cdot \nabla T) - Q_v = 0 \quad (4)$$

Boundary conditions are used to model convective (when the vacuum is broken) and radiative losses such that the boundary flux density $q_{\text{conv+rad}}$ is:

$$q_{\text{conv+rad}}(T) = h_{\text{conv}}(T)(T - T_{ch}) + \sigma_{SB} \Xi(T^4 - T_{ch}^4) \quad (5)$$

where T , T_{ch} , h_{conv} , σ_{SB} and Ξ represent the temperature of the computed point [K], the temperature of the vacuum chamber (the initial temperature is provided by thermocouples), the convective coefficient of air [$\text{W m}^{-1} \text{K}^{-1}$] when the vacuum is broken, the Stefan–Boltzmann constant ($\sigma_{SB}=5.67 \times 10^{-8} \text{ J K}^{-4} \text{ m}^{-2} \text{ s}^{-1}$) and the emissivity of the aluminium surface. In this study, the convective coefficient h_{conv} can be assumed constant because the convection occur only at low temperatures.

In the solidification range (between the solidus and the liquidus – Zain-Ul-Abdein et al., 2009 provides: $587\text{--}644^\circ\text{C}$) the heat capacity of the alloy undergoes a discontinuity (cf. Fig. 10), inducing a latent heat of fusion L_f^m . During the computation, the liquid fraction f_L provides an enthalpy contribution $H_{S-L} = f_L \cdot L_f$ in Eq. (4). For an aluminium alloy L_f it is about $4 \times 10^5 \text{ J kg}^{-1}$ according to Gandin (2000). To have a correct treatment of this discontinuity an enthalpy formulation is used in Sysweld FE software (rather the well known " C_p equivalent method") and the non-linear resolution for this unstationary problem is solved relying to an implicit backward Euler finite element time-discretisation and coupled Broyden–Fletcher–Goldfarb–Shanno/conjugate gradient algorithm.

4.2. Finite element model

The electron beam (EB) welding process induces thermal gradient in and near the MZ, where a high mesh density is required. A

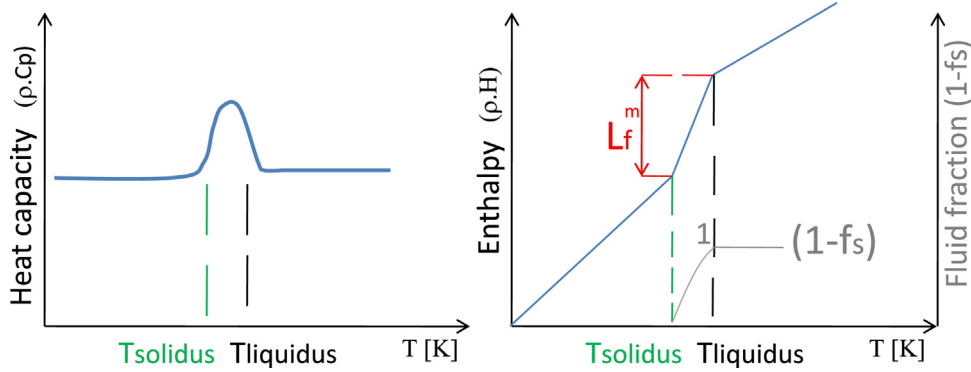


Fig. 10. Schematic representation of the “equivalent C_p ” method and the enthalpic formulation. f_s represents the fraction of solid during computation and L_f^m the latent heat fusion.

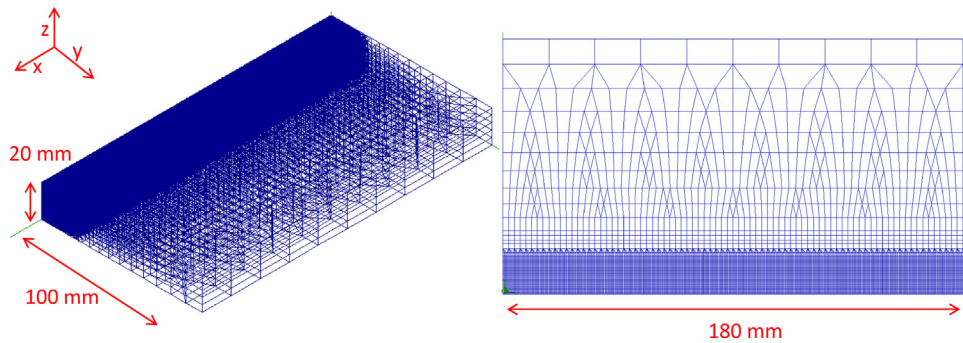


Fig. 11. Meshing used for the thermal computation.

progressive meshing is used to reduce the mesh size where fine elements are not required. A majority of hexahedral 8-nodes elements and some linear prismatic 6-nodes element are used (Fig. 11). The mesh is composed of 519,565 elements and 487,321 nodes. The dimensions of the smallest element are $0.5 \text{ mm} \times 0.5 \text{ mm} \times 0.5 \text{ mm}$ in the MZ.

Material's data were obtained according to Simar et al. (2006)'s work while the convective and radiative coefficients were deduced from Zain-Ul-Abdein et al. (2010) work on 6056 alloy: (i) $h_{\text{conv}} = 0$ in vacuum and $15^{-1} \text{ W K m}^{-1}$ in air, (ii) $\Xi = 0.08$ (polished surface).

In view of cross sections of Fig. 2, an equivalent 3D volumetric conical heat source have been chosen (Fig. 13) as in Zain-Ul-Abdein et al. (2010). In this model, a Gaussian energy repartition is assumed on the upper surface with a linear decline through the thickness.

The net energy Q_0 absorbed by the plate is given by: $Q_0 = \eta UI = \int_Q Q_V dV$ where U , I , Q_V , and dV represents the voltage [V], the intensity [A] of the welding device and the total volumetric energy [W m^{-3}]. The efficiency η has been adjusted: it represents the intrinsic energy loss in welding device but also by the MZ pool and plasma movement, the reflection in the chamber, the heat transferred out of the plate (weld-through). Here, the volumetric energy absorbed into the plate Q_V can be written as a function of the maximum energy density Q_c for every plane z according to “truncated Gaussian” distribution of radius $R_c(z)$ (the radius is defined here by $Q_V(R_c) = 0.05 \cdot Q_c$):

$$Q_V(r, z) = Q_c \cdot \exp \left(-\frac{3r^2}{R_c(z)^2} \right) \quad (6)$$

The conservation of energy provides in the source volume V_S . Zain-Ul-Abdein et al. (2010) show that the knowledge of the $R_c(z)$

expression based on the upper and lower radius source $r_e - r_i$ and the distribution (r, z) of energy density Q_V provide:

$$Q_V(r, z) = \frac{9\eta UI}{\pi(1 - \exp(-3))} \frac{\exp(-3r^2/r_c(z)^2)}{(z_e - z_i)(r_e^2 + r_e r_i + r_i^2)} \quad (7)$$

4.3. Thermal results

The heat source modelled in Eq. (7) has been implemented in the FE software Sysweld thanks to a Fortran subroutine. Thus, for each time and integration point the volumetric heat source can be integrated in the FE resolution. In Eq. (7), the quantity $z_e - z_i$ is equal to the plate thickness, the electrical tension U and intensity I are directly obtained from the experimental device parameters.

The constants r_e , r_i and η were fitted to get a MZ that is as identical as in cross sections of Fig. 2 and also to have a best fit between numerical thermal histories and thermocouples measurements. Thus, one gets $r_e = 0.9 \text{ mm}$, $r_i = 0.48 \text{ mm}$ and $\eta = 0.86$.

On the results shown in Fig. 13 the red colour represents the solidus temperature, its shape have been plotted and confronted with the experimental contour in the same figure. We can see that the MZ is well represented in the lower half thickness but, in the upper part, a discrepancy occurs, probably due to surface tension effects (fluid flow is not explicitly taken into account in our simulations).

Nevertheless, the time-temperature curves presented in Fig. 12 show that the heating and cooling kinetics are very well represented for the upper and lower surfaces. The heating rates and the maximum temperature greatly dependent on material properties and the calibration of the heat source. The maximum error is obtained for TC4 ($\approx 7\%$ on maximal temperature) which is the

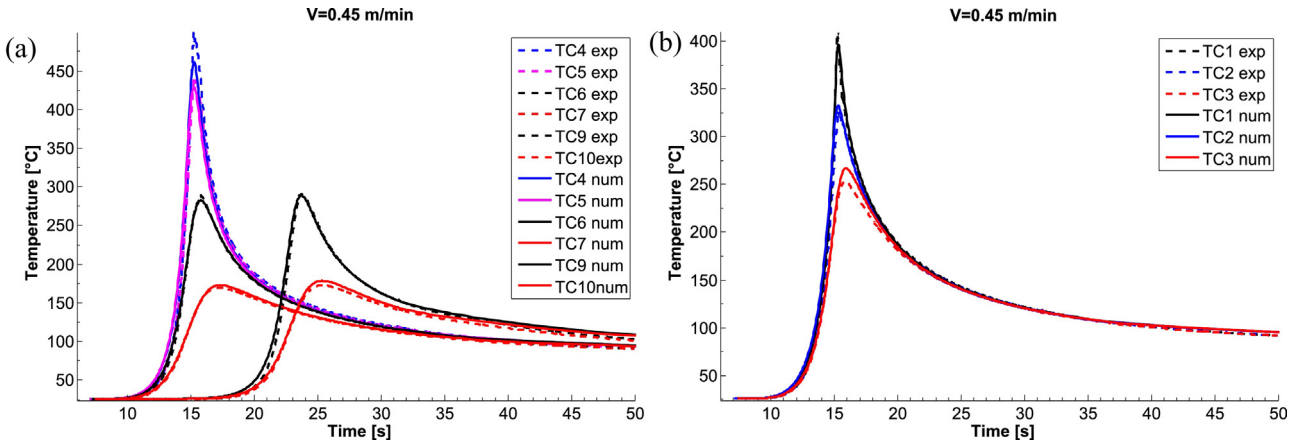


Fig. 12. Comparison between time-temperature histories for the plate $V=0.45 \text{ m/min}$, (a) on the upper and (b) the lower surface. For exact positioning see Fig. 1.

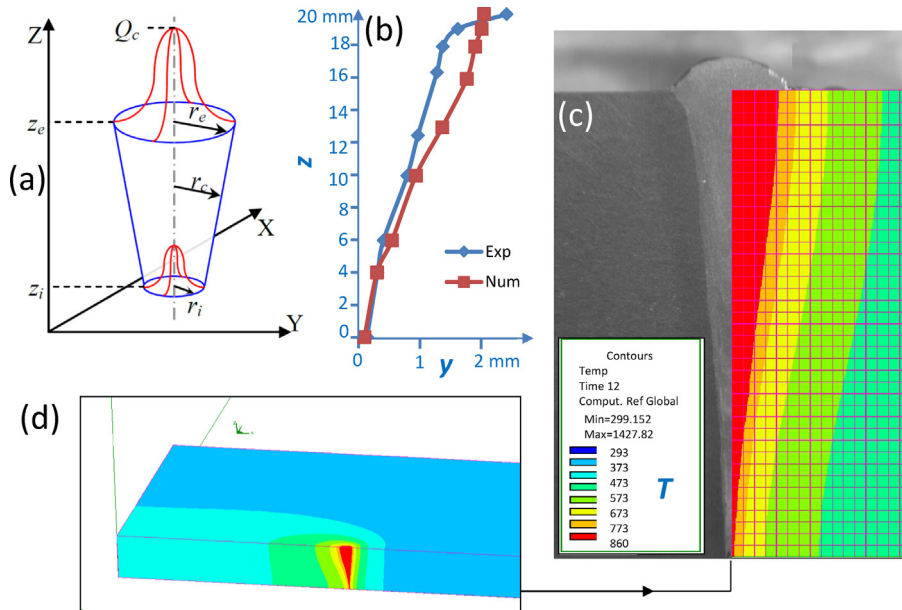


Fig. 13. (a) Equivalent conical heat source, (b) comparison between numerical and experimental molten zone boundary and (c) associated macrography. Overview of the FE thermal results for a welded plate ($V=0.45 \text{ m/min}$). (For interpretation of the references to colour in text, the reader is referred to the web version of the article.)

closest from the MZ. The cooling rate is dependent on boundary conditions and this effect is well represented too.

5. Residual elastic strains

5.1. Model

The approach used here is based on isokinetic dissolution model from Myhr and Grong (1991) work coupled with a hardening model calibrated in a previous study (Maisonnette et al., 2015) on non-isothermal treatments (representative of time-temperature histories given in Fig. 12). This approach uses two fictitious proportions of phases for the AA6061: a “hard” phase p_1 (equal to 1 for the optimised precipitation T6 state) and a “soft” phase $p_2 = 1 - p_1$ associated to the O state (state where the hardening precipitates $\beta'' - \beta$ are dissolved). Note that, in the MZ, only the microstructural degradation due to the precipitation state is modelled. Indeed, Starink et al. (2008) have shown that for age hardening aluminium alloys, the evolution of the precipitation state during welding is the main factor influencing the strength drop (the grain size strengthening

is generally less than 10 MPa). A recent contribution of the authors (Bardel et al., 2016), where massive microhardness measurements were performed in HAZ and MZ, confirm this study. According to Myhr and Grong (1991), the generation of the soft phase that can be written as:

$$\left\{ \begin{array}{l} \dot{p}_2 = \frac{n \cdot p_2^{(1-1/n)}}{t^*} \\ n = 0.5 - a \cdot p_2^b \\ t^* = t_r^* \cdot \exp \left[\left(\frac{Q_s}{nR} + \frac{Q_d}{R} \right) \left(\frac{1}{T} - \frac{1}{T_r} \right) \right] \end{array} \right. \quad (8)$$

where $a = 0.394$, $b = 0.107$, $Q_s = 30 \text{ kJ/mol}$, $Q_d = 130 \text{ kJ/mol}$, $t_r^* = 600 \text{ s}$ and $T_r = 375^\circ\text{C}$ are some constants fitted in Hirose et al. (2000) thanks to hardness measurements. Thus, the thermo-mechanical behaviour $\sigma_{eq}(T)$ can be deduced from the phase proportions thanks to a mixing law:

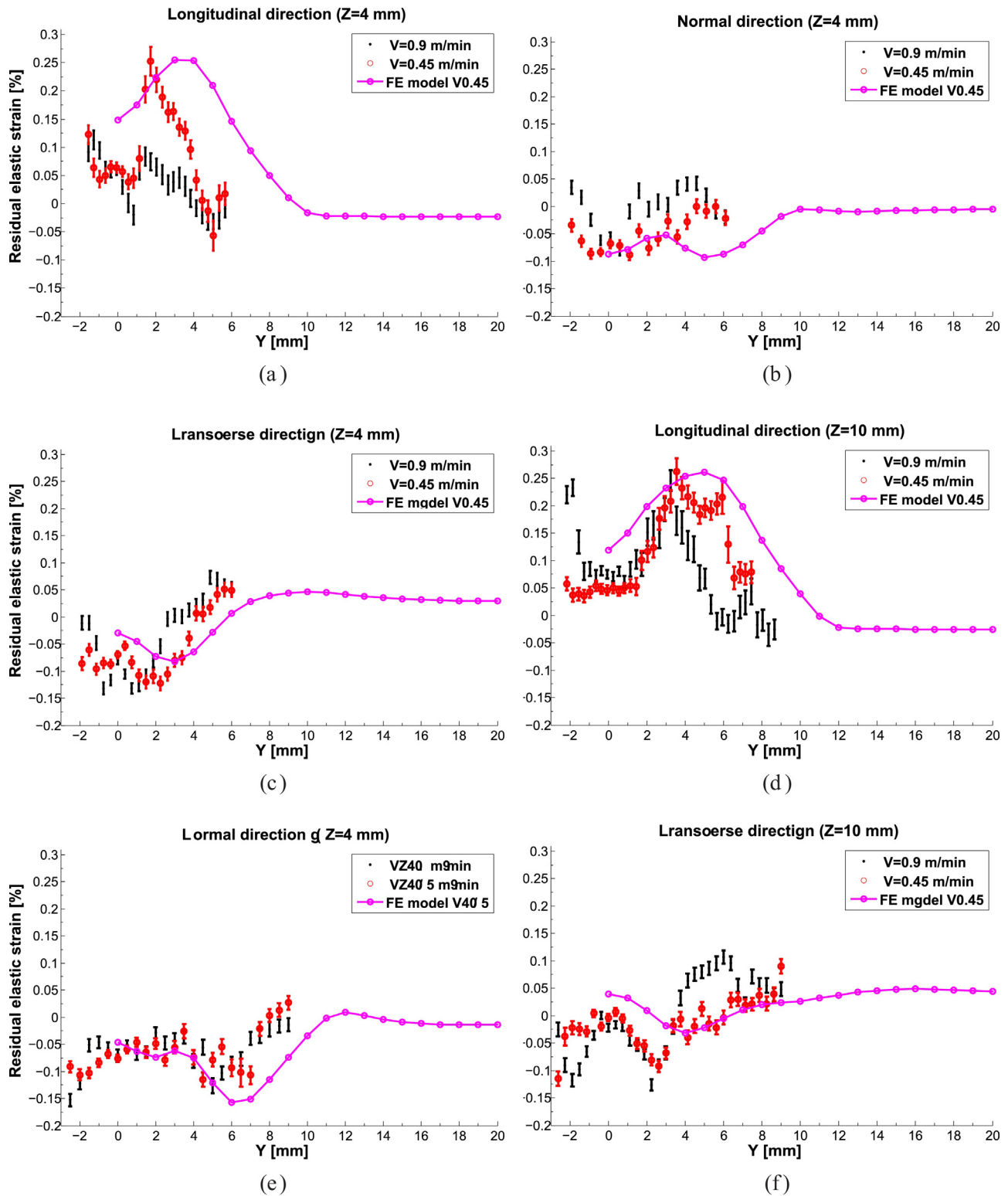


Fig. 14. Residual elastic deformation for a transverse weld line at 4 mm from the lower surface for the (a) longitudinal, (b) normal and (c) transverse direction. Confrontation between numerical and experimental results for a welding velocity of $V=0.45 \text{ m/min}$. Additional experimental results are shown with $V=0.9 \text{ m/min}$ to quantify the influence of velocity. Same results at 10 mm from the lower surface for the (d) longitudinal, (e) normal and (f) transverse direction.

$$\sigma_{eq}(T) = p_2 \cdot \sigma_0(T) + (1 - p_2) \cdot \sigma_{T6}(T) \quad (9)$$

where $\sigma_0(T)$ and $\sigma_{T6}(T)$ are the tensile curves of the T6 and O states. They are fitted in [Maisonneuve et al. \(2015\)](#) by inverse method on

tensile tests to find the tensile behaviour of the AA6061-T6 alloy with temperature.

The boundary conditions are chosen to prevent rigid body motion by blocking the displacements (*cf.* Fig. 11): U_y in the symmetric plane, U_z for three extreme nodes in the lower surface and

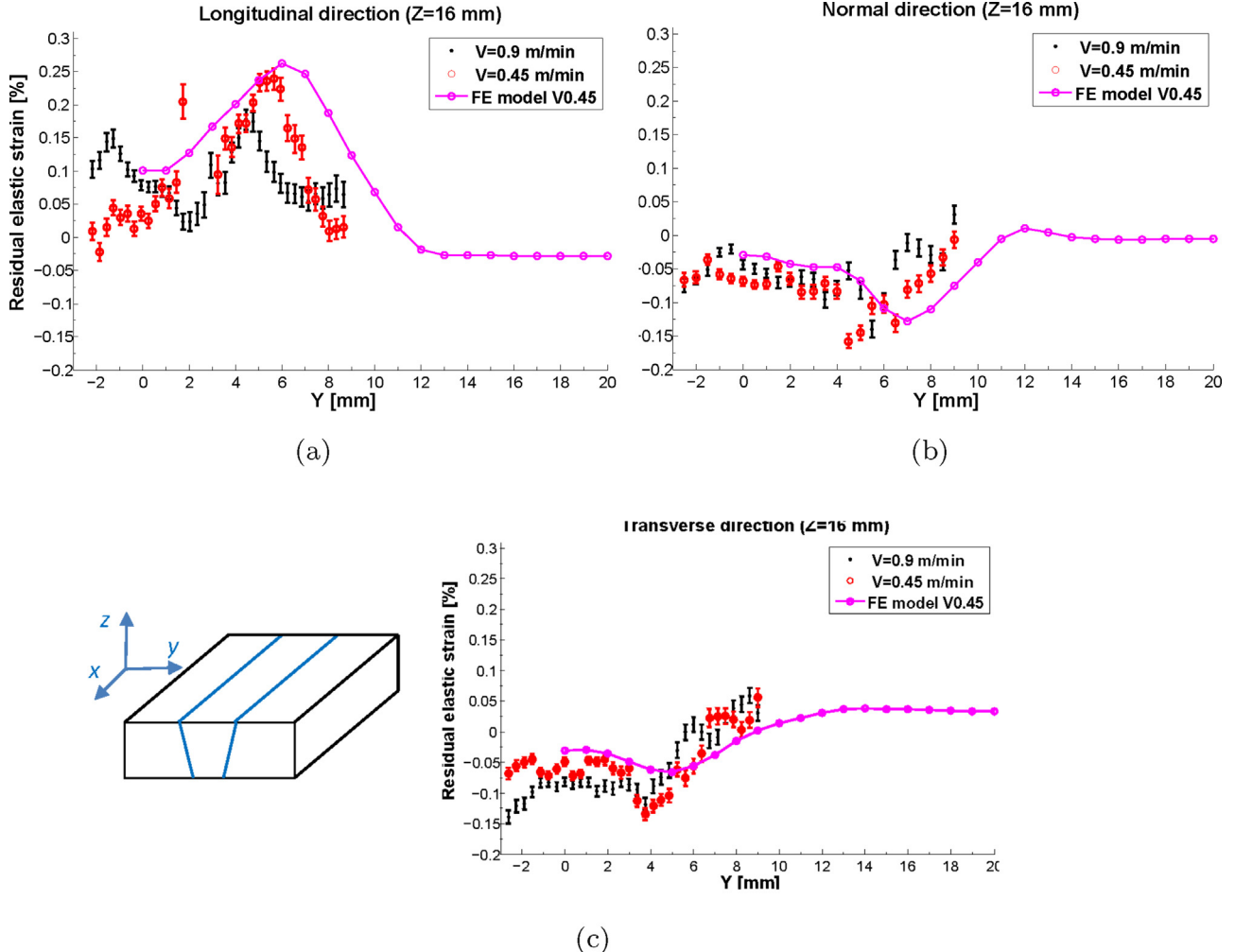


Fig. 15. Residual elastic deformation for a transverse weld line at 16 mm from the lower surface for the (a) longitudinal, (b) normal and (c) transverse direction. Confrontation between numerical and experimental results for a welding velocity of $V = 0.45$ m/min. Additional experimental results are shown with $V = 0.9$ m/min to quantify the influence of velocity.

U_x for the two extreme nodes of the lower line that is on the edge 100 mm (position $x=0$).

5.2. Results

The thermo-metallurgical simulation is performed on the finite element mesh (121,318 elements, 108,474 nodes and the smallest mesh size is 1 m^3) that have been chosen to reduce the computation time while having acceptable results (only the numeric MZ root is less accurate). The same equivalent heat source boundary condition that the one presented in the previous paragraph is considered. To compare the residual elastic deformations predicted by the simulation with neutron diffraction results, an averaging was carried out in accordance with the gauge volumes presented in Fig. 6.

The results are compared with measurements in Figs. 14 and 15 for transverse lines across the weld section. Note that the metallurgical model proposed for the 6061-T6 alloy coupled with the thermal simulation provides a good correlation with the residual deformations given by the neutron diffraction technique for all investigated directions. Note that the drop close to the centre of the weld (typical "M" shape due to the softening by dissolution, Sonne et al., 2013) is well captured by the simulation.

Nevertheless, it should be noted that even if the molten zone is well represented by the thermal model (see Fig. 13) a slight

transverse shift was obtained in Figs. 14 and 15 between experiments and simulations.

This effect can be due to several reasons:

- the use of a rather crude and simple dissolution model, which tend to reduce the HAZ,
- a shift in the sample alignment, and
- the evolution of the mechanical properties in the MZ (transition in the semi-solid zone) has not been considered (for more details see for example, Giraud et al., 2012): the mechanical properties of the solid fraction are computed thanks to (9) and the stresses are relaxed in the fluid part.

In view of the symmetry of the results regarding to the weld centre (0 point on the curves in Figs. 14 and 15) the second reason can be reasonably rejected. A possible improvement would therefore be the replacement of the phenomenological Maisonneuve et al. (2015) approach by a more physical model such as recently proposed by Bardel et al. (2014). The fitting of the heat source could also be improved by taking into account the effects of surface tension close to the surface of the welds. In addition, it should be noticed that the work hardening model used in this study is assumed isotropic, but the thermal cycle introduce a mechanical cycle that could be apprehended for this alloy more accurately with the more

advanced mixed work hardening model presented by Bardel et al. (2015).

6. Conclusions

An investigation that aims to study the consequences of an electron beam welding on a 6061 aluminium alloy (initially in the T6 state) has been presented. In this paper, an instrumented fusion line has been performed together with macrographs in order to study the thermal field encountered during the process. These data were used to calibrate a thermal finite elements model of the process. Then, scanning electron microscopy characterisations were also performed to discuss the welding influence on grain size/shape as well as coarse precipitation state.

A coupling between a simple metallurgical model (microstructural and mechanical evolution based on precipitates dissolution) and a thermal analysis has shown that an isokinetic approach can provide relatively good results in terms of residual elastic deformations for a single-pass welding process.

This validation was performed by using a neutrons diffraction technique on the SALSA device (ILL). The residual elastic strains exhibit typical "M" profile (for age hardening aluminiums) in the longitudinal direction, which validates the measurement reported in the literature where similar observations were performed.

Acknowledgements

The authors gratefully acknowledge AREVA and SAFRAN for partial funding of this work within the framework of the "Life extension and manufacturing processes" teaching and research Chair and the French Atomic Energy Commission (CEA) for industrial and financial support, especially F. Bourlier, P. Gilles and J. Garnier. P. Chaudet, P.C. Shao and Z. Szaraz are also thanked for their technical advices. The authors would like to acknowledge the Institut Laue Langevin, Grenoble, France, for the provision of beam time.

References

- Acvedo, C., Evans, A., Nussbaumer, A., 2012. Neutron diffraction investigations on residual stresses contributing to the fatigue crack growth in ferritic steel tubular bridges. *Int. J. Press. Vessel. Pip.* 95, 31–38.
- Bardel, D., Nelias, D., Chaise, T., Fontaine, M., Perez, M., Bourlier, F., Garnier, J., 2016. Mechanical properties of a 6061-T6 weld joint: finite elements based on microstructure versus digital image correlation tensile test (submitted for publication).
- Bardel, D., Perez, M., Nelias, D., Dancette, S., Chaudet, P., Massardier, V., 2015. Cyclic behaviour of a 6061 aluminium alloy: coupling precipitation and elastoplastic modelling. *Acta Mater.* 83, 256–268.
- Bardel, D., Perez, M., Nelias, D., Deschamps, A., Hutchinson, C., Maisonneuve, D., Chaise, T., Garnier, J., Bourlier, F., 2014. Coupled precipitation and yield strength modelling for non-isothermal treatments of a 6061 aluminium alloy. *Acta Mater.* 62, 129–140.
- Boulnat, X., Perez, M., Fabregue, D., Douillard, T., Mathon, M.-H., de Carlan, Y., 2014. Microstructure evolution in nano-reinforced ferritic steel processed by mechanical alloying and spark plasma sintering. *Metall. Mater. Trans. A* 45A, 1485–1497.
- Calcagnotto, M., Ponge, D., Demir, E., Raabe, D., 2010. Orientation gradients and geometrically necessary dislocations in ultrafine grained dual-phase steels studied by 2D and 3D EBSD. *Mater. Sci. Eng. A* 527 (1011), 2738–2746.
- Chobaut, N., Carron, D., Arsne, S., Schloth, P., Drezet, J.-M., 2015. Quench induced residual stress prediction in heat treatable 7xxx aluminium alloy thick plates using Gleeble interrupted quench tests. *J. Mater. Process. Technol.* 222, 373–380.
- Costa, J., Pires, J., Antunes, F., Nobre, J., Borrego, L., 2010. Residual stresses analysis of ND-YAG laser welded joints. *Eng. Fail. Anal.* 17, 28–37.
- Debroy, T., David, S., 1995. Physical processes in fusion welding. *Rev. Mod. Phys.* 67, 85–112.
- Delannay, L., Mishin, O., 2013. Crystal plasticity modeling of the through-thickness texture heterogeneity in heavily rolled aluminum. *Key Eng. Mater.* 554, 1189–1194.
- Deplus, K., Simar, A., van Haver, W., de Meester, B., 2011. Residual stresses in aluminium alloy friction stir welds. *Int. J. Adv. Manuf. Technol.* 56, 493–504.
- Drezet, J., Pirling, T., Jaquierod, C., 2012. Residual stresses in as-cast billets: neutron diffraction measurement and thermomechanical modeling. In: Carlos, E., Suarez (Eds.), *Light Metals 2012*.
- Gandin, C.-A., 2000. From constrained to unconstrained growth during directional solidification. *Acta Mater.* 48, 2483–2501.
- Giraud, E., Suéry, M., Coret, M., 2012. High temperature compression behavior of the solid phase resulting from drained compression of a semi-solid 6061 alloy. *Mater. Sci. Eng. A* 532, 37–43.
- Goldak, J., Chakravati, A., Bibby, M., 1984. A new finite element model for welding heat sources. *Metall. Trans.* 15B, 299–305.
- Hirose, A., Kobayashi, K., Yamaoka, H., Kurosawa, N., 2000. Evaluation of properties in laser welds of A6061-T6 aluminium alloy. *Weld. Int.* 14 (6), 431–438.
- Hunt, J., 1984. Steady state columnar and equiaxed growth of dendrites and eutectic. *Mater. Sci. Eng.* 65, 75–83.
- Maisonneuve, D., Bardel, D., Nelias, D., Suery, M., 2015. Mechanical Behaviour at High Temperature as Induced During Welding of a 6xxx Series Aluminium Alloy (submitted for publication).
- Mokadem, S., Bezencon, C., Hauert, A., Jacot, A., Kurz, W., 2007. Laser repair of superalloy single crystals with varying substrate orientations. *Metall. Mater. Trans. A* 38A, 1500–1510.
- Myhr, O., Grong, O., 1991. Process modelling applied to 6082-T6 aluminium weldments: I. Reaction kinetics. *Acta Metall. Mater.* 39, 2963–2702.
- Perez, M., Dumont, M., Acevedo-Reyes, D., 2008. Implementation of the classical nucleation theory for precipitation. *Acta Mater.* 56, 2119–2132.
- Pirling, T., Bruno, G., Withers, P., 2006. SALSA: advances in residual stress measurement at ILL. *Mater. Sci. Forum* 524–525, 217–222.
- Rappaz, M., Gandin, C., 1993. Probabilistic modelling of microstructure formation in solidification processes. *Acta Metall. Mater.* 2, 345–360.
- Rossini, N., Dassisti, M., Benyounis, K., Olabi, A., 2012. Methods of measuring residual stresses in components. *Mater. Des.* 35, 572–588.
- Shen, Y., Morgeneyer, T., Garnier, J., Allais, L., Helfen, L., Crépin, J., 2013. Three-dimensional quantitative *in situ* study of crack initiation and propagation in AA6061 aluminum alloy sheets via synchrotron laminography and finite-element simulations. *Acta Mater.* 61, 2571–2582.
- Simar, A., Bréchet, Y., de Meester, B., Denquin, A., Gallais, C., Pardoën, T., 2012. Integrated modeling of friction stir welding of 6xxx series al alloys: process, microstructure and properties. *Prog. Mater. Sci.* 57, 95–183.
- Simar, A., Lecomte-Beckers, J., Pardoën, T., de Meester, B., 2006. Effect of boundary conditions and heat source distribution on temperature distribution in friction stir welding. *Sci. Technol. Weld. Join.* 11, 170–177.
- Sonne, M., Tutum, C., Hattel, J., Simar, A., de Meester, B., 2013. The effect of hardening laws and thermal softening on modeling residual stresses in FSW of aluminum alloy 2024-T3. *J. Mater. Process. Technol.* 213, 477–486.
- Starink, M., Deschamps, A., Wang, S., 2008. The strength of friction stir welded and friction stir processed aluminium alloys. *Scr. Mater.* 58, 377–382.
- Traida, A., Roger, F., 2011. A computational investigation of different helium supplying methods for the improvement of GTA welding. *J. Mater. Process. Technol.* 211, 1553–1562.
- Traida, A., Roger, F., Schroeder, J., Guyot, E., Marlaud, T., 2013. On the effects of gravity and sulfur content on the weld shape in horizontal narrow gap GTAW of stainless steels. *J. Mater. Process. Technol.* 213, 1128–1138.
- Wang, N., Mokadem, S., Rappaz, M., Kurz, W., 2004. Solidification cracking of superalloy single- and bi-crystals. *Acta Mater.* 52, 3173–3182.
- Withers, P., 2007. Mapping residual and internal stress in materials by neutron diffraction. *C.R. Phys.* 8, 806–820.
- Zain-Ul-Abdein, M., Nelias, D., Jullien, J., Deloison, D., 2009. Prediction of laser beam welding-induced distortions and residual stresses by numerical simulation for aeronautic application. *J. Mater. Process. Technol.* 209, 2907–2917.
- Zain-Ul-Abdein, M., Nelias, D., Jullien, J., Deloison, D., 2010. Experimental investigation and finite element simulation of laser beam welding induced residual stresses and distortions in thin sheets of AA 6056-T4. *Mater. Sci. Eng. A* 527, 3025–3039.